

Experimental study of Raman-active two-level systems and the boson peak in LaF₃-doped fluorite mixed crystals

J. J. Tu and A. J. Sievers

Laboratory of Atomic and Solid State Physics and Cornell Center for Materials Research, Cornell University, Ithaca, New York 14853-2501

(Received 6 March 2002; revised manuscript received 21 May 2002; published 19 September 2002)

A broad spectral distribution of two-level systems (TLS) displaying only A_{1g} symmetry, not E_g or T_{2g} , is observed in the low-frequency, low-temperature Raman spectra of fluorite single crystal hosts doped with large amounts of LaF₃. The observed range of each TLS spectrum is found to be independent of the dopant concentration although each of the three crystalline hosts, CaF₂, SrF₂, and BaF₂, displays a slightly different cutoff frequency. In a somewhat higher frequency range but still far below the Brillouin Zone TA phonon mode frequency, a boson peak, showing E_g symmetry, is also observed and its strength is proportional to the defect-induced vibrational Raman activity for the three crystal lattices. A surprising property is that for all three host crystals the boson peak center frequency increases with increasing lattice disorder. The strengths of the TLS spectra show distinctively different La³⁺ concentration dependencies in each host, which is also different from that observed for the boson peaks. By comparing the density of state of TLS derived from the Raman scattering to the \bar{P} density of states value determined from the earlier specific heat measurements, the number density of Raman-active TLS is separated from the coupling coefficient. When the total number density of Raman-active TLS is examined versus different physical properties it is found that lattice disorder, not the LaF₃ concentration per se, is the important variable. The experimental results are consistent with a model where the TLS number density is controlled by the law of mass action with the “effective” temperature associated with the production of TLS determined by the frozen-in lattice disorder. Good agreement is found for the number density of TLS versus concentration as determined from the present Raman scattering data and the previous far infrared measurements when the far infrared dipole moment is used as a single fitting parameter. However, in contrast with the far infrared studies, no TLS excited state transitions are observed in Raman scattering. The overall findings from this study suggest that the Raman and infrared active TLS distributions, which extends up to about 2 meV, are associated with extended entities.

DOI: 10.1103/PhysRevB.66.094206

PACS number(s): 61.43.Fs, 63.50.+x, 78.30.-j

I. INTRODUCTION

Although the early Raman scattering measurements of the vibrational properties of defects in fluorite crystals focused on their low-temperature properties,¹⁻³ the next decade gave rise to a number of high-temperature Raman studies,⁴⁻⁷ mainly because both pure and doped fluorite crystals exhibit superionic conduction behavior above a certain temperature T_c , which is well below the melting point. This transition has been identified with the effective melting of the anion sublattice. In recent years, the low-temperature properties of these fluorite mixed crystals have again attracted much attention since the discovery of a continuous distribution of two-level systems (TLS) in the low-temperature specific heat of yttrium-stabilized cubic zirconia.⁸ A similar TLS behavior was first found in fluorite mixed crystals of the type $(MF_2)_{1-x}(RF_3)_x$, where M is an alkaline-earth ion and R is a rare-earth ion by means of microwave resonant absorption measurements.⁹ Because of the apparent similarity between these excitations and those previously identified in glasses¹⁰⁻¹³ and the simplicity of the fluorite crystal structure, the low-temperature dynamical properties of the mixed fluorite crystals have now been probed with a variety of experimental techniques. These include thermal,¹⁴ mechanical,^{15,16} far-infrared absorption spectroscopy,¹⁷⁻¹⁹ Raman scattering,²⁰⁻²² and the infrared (IR) persistent hole

burning technique.²³ In addition to a TLS spectrum there is some evidence that these fluorite mixed crystals also display a Raman-active boson peak in the vibrational region,^{24,25} very similar to the boson peak found in glasses.²⁶⁻²⁹ Recent theoretical studies,^{30,31} based on models of random force constants in crystals, suggest that this feature may follow directly from lattice disorder so there is added interest in testing this idea experimentally.

It is important to recognize that thermal and mechanical techniques probe the low-frequency dynamics of TLS in fluorite mixed crystals while far-IR absorption and Raman scattering probe their high-frequency properties. The detailed low-temperature Raman scattering study of heavily doped mixed fluorite crystals presented here complements the earlier far-IR absorption studies^{18,19} and brings forth a number of important general features of TLS. One is that the Raman scattering from TLS only exists up to the meV energy range similar to that found for the far-IR measurements; another is that the total number density of Raman-active TLS can be identified and estimated. Surprisingly this total number density of TLS not only depends on the LaF₃ dopant concentration but also on the resultant frozen-in lattice disorder. By also incorporating x-ray measurements into this study it is demonstrated that the width of the Raman-active T_{2g} phonon mode can be used to identify an “effective disorder temperature” for each crystal. This effective disorder temperature

TABLE I. Identification of the mixed crystal fluorite samples. Column 1, the impurity concentration as determined from x-ray fluorescence; column 2, the sample code identifier; and column 3, the spectral density $g_{\text{TLS}}^{(0)}$ obtained from the Raman scattering measurements. This last result can be compared with \bar{P} . The samples were either purchased commercially from Optivac (Brookfield, MA), or grown for us by Campbell, University of Canterbury, New Zealand.

Sample	Code	$g_{\text{TLS}}^{(0)}$ ($10^{32} \text{ erg}^{-1} \text{ cm}^{-3}$)
(CaF ₂) _{0.99} (LaF ₃) _{0.01}	CAL.01.JC.1	0.0
(CaF ₂) _{0.95} (LaF ₃) _{0.05}	CAL.05.JC.1	2.1
(CaF ₂) _{0.90} (LaF ₃) _{0.10}	CAL.10.JC.1	2.9
(CaF ₂) _{0.80} (LaF ₃) _{0.20}	CAL.20.OP.1	3.8
(CaF ₂) _{0.67} (LaF ₃) _{0.33}	CAL.33.OP.1	4.0
(CaF ₂) _{0.56} (LaF ₃) _{0.44}	CAL.44.OP.1	3.9
(BaF ₂) _{0.95} (LaF ₃) _{0.05}	BAL.05.JC.1	0.73
(BaF ₂) _{0.85} (LaF ₃) _{0.15}	BAL.15.JC.1	1.4
(BaF ₂) _{0.75} (LaF ₃) _{0.25}	BAL.25.JC.1	2.2
(BaF ₂) _{0.65} (LaF ₃) _{0.35}	BAL.35.JC.1	2.7
(BaF ₂) _{0.55} (LaF ₃) _{0.45}	BAL.45.JC.1	3.1
(SrF ₂) _{0.95} (LaF ₃) _{0.05}	SRL05.OP.1	0.22
(SrF ₂) _{0.90} (LaF ₃) _{0.10}	SRL10.JC.1	0.46
(SrF ₂) _{0.85} (LaF ₃) _{0.15}	SRL15.OP.1	0.65
(SrF ₂) _{0.75} (LaF ₃) _{0.25}	SRL25.OP.1	0.92
(SrF ₃) _{0.65} (LaF ₃) _{0.35}	SRL35.OP.1	1.14
(BaF ₂) _{0.70} (SrF ₂) _{0.30}	BASR.30.OP.1	0.0
(BaSrF ₂) _{0.99} (LaF ₃) _{0.01}	BASRLA.01.JC.1	0.82
(BaSrF ₂) _{0.95} (LaF ₃) _{0.05}	BASRLA.05.JC.1	3.44

plays an important role in determining the total number density of Raman-active TLS for the LaF₃ doped crystals. Here it is shown that the unusual concentration dependence measured for the Raman-active TLS can be characterized by the law of mass action when this frozen-in disorder temperature is used in place of the sample temperature. Since the strength of the boson peak is found to scale with the LaF₃ concentration while the TLS total number density does not, our experiments demonstrate that these two Raman signatures of the disordered state are uncorrelated.

Section II outlines the experimental details, focusing on the x-ray and Raman procedures. Section III presents the experimental results for the LaF₃-doped crystals. These include the x-ray measurements, and low-temperature Raman measurements spanning the vibrational region, the boson peak, and the low-lying TLS. The data analysis and discussion are presented in some detail in Sec. IV. Here an estimation of the total Raman-active TLS number density is made for each crystal. The summary and conclusions in Sec. V complete the picture.

II. EXPERIMENTAL DETAILS

The (MF₂)_{1-x}(LaF₃)_x samples, where M=Ca²⁺, Sr²⁺, Ba²⁺, and 0 ≤ x ≤ 0.45, and the doped BaSrF₂ alloy crystal samples used for this work are listed in Table I. The samples

were either purchased commercially from Optivac (Brookfield, MA) or grown for us by Campbell. The Raman data obtained on samples from the two different sources are consistent with each other, and therefore, no distinction will be made between them in the Results section.

The impurity concentration is determined using x-ray fluorescence produced by an electron microprobe. The measurements were performed at Cornell using a General Electric OL733 machine. This analysis technique could determine the molar ratio of the host to dopant ions and this is all that is required to deduce the dopant concentration. Its value is double checked with x-ray power diffraction measurements.

X-ray diffraction of the samples was used for two purposes: (1) to insure that the samples were single crystals even at the highest dopant concentrations and (2) to determine the lattice constant, when in powder form. The x-ray diffraction of single crystal samples was carried out in Laue backscattering geometry using a grid-wire detector. Crystallographic axes are found in this way and single crystal samples are then cut into approximately 5 mm cubes along ⟨100⟩, ⟨011⟩, and ⟨01-1⟩ cubic axis using a diamond saw. The sample cubes are polished mechanically until optical quality is achieved. Small pieces of the samples are ground into fine powders and x-ray diffraction is done using a 2θ x-ray diffractometer. These measurements were also performed at Cornell.

The Raman spectra have been measured with a Dilor XY 211 system using the 514.532 nm excitation line of an argon ion laser. For each experimental run, the monochromator was properly calibrated with the laser line so that the zero position of the monochromator was centered on the laser frequency. The liquid N₂ cooled charge coupled device (CCD) detector consists of an array of 512 × 1024 photodiodes and this allows a wide frequency range of more than 700 cm⁻¹ to be covered at once. In total, eight 90° scattering configurations are possible and some of them yield the same results. Four 90° scattering configurations are actually used: ⟨001⟩⟨001⟩ gives the 4/3 E_g + A_{1g} spectrum; ⟨001⟩⟨011⟩ the T_{2g} spectrum; ⟨011⟩⟨01-1⟩ the E_g spectrum, and ⟨011⟩⟨011⟩ the 1/3 E_g + T_{2g} + A_{1g} spectrum. Three configurations are used to separate the three different contributions and the fourth one is used to check if the assignments are consistent.

An Oxford Variox optical cryostat is used for the low-temperature measurements. The samples can either be immersed in superfluid helium 4 or in helium gas. The lowest temperature accessible with pumped helium 4 is 1.4 K. The temperatures are monitored by three temperature sensors: a commercially calibrated rhodium-iron thermocouple placed on the heat exchanger near the sample, a commercially calibrated Lakeshore silicon diode thermocouple mounted on the sample holder, and a 1000Ω Allen Bradley resistor also mounted on the sample holder. The most accurate temperature sensor is the Si-diode thermocouple on the sample holder and the other thermometers are used as checks. An Oxford ITC503 temperature controller is used to fix the temperature of the heat exchanger at desired temperatures.

Each spectrum is typically taken in a 600 s duration using 200 mW of laser power with 2.10 cm⁻¹ resolution. Both Stokes and anti-Stokes spectra have been recorded at each

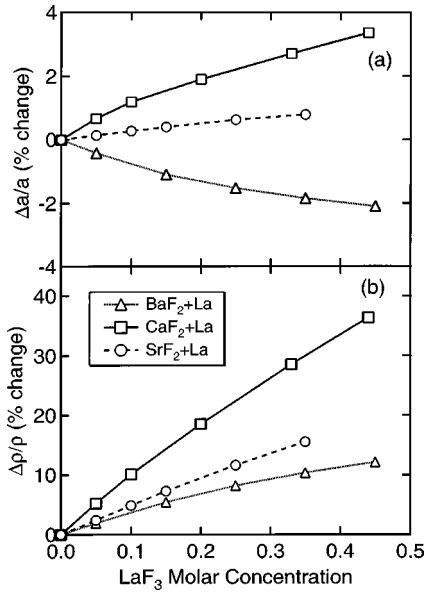


FIG. 1. LaF₃ concentration dependence of the percentage changes in lattice constant and density in three fluorite mixed crystal systems. (a) The percentage change $\Delta a/a$ and (b) the percentage change in $\Delta\rho/\rho$. Squares for $(\text{CaF}_2)_{1-x}(\text{LaF}_3)_x$, circles for $(\text{SrF}_2)_{1-x}(\text{LaF}_3)_x$, and triangles for $(\text{BaF}_2)_{1-x}(\text{LaF}_3)_x$.

temperature. Low-temperature readings were checked by comparing the temperature values obtained from the Stokes and anti-Stokes spectra with the sample thermometer reading. In addition, no change was observed in the thermometer readings with the laser on or off, thus no laser-induced thermal heating of the samples is observed in these experiments. To check for thermal hysteresis, the temperature dependence of each sample is repeated twice: once with increasing temperatures and then with decreasing temperatures. The combination of these techniques shows that the temperature measured by the thermometer is the actual temperature of the scattering volume, even at low temperatures. In each case several spectra have been averaged to eliminate the effects of cosmic rays and other noise factors.

III. EXPERIMENTAL RESULTS ON LaF₃-DOPED FLUORITE MIXED CRYSTALS

A. X-ray and density measurements

X-ray powder diffraction results for the LaF₃ concentration dependence of the percentage change in lattice constant and density for the three fluorite mixed crystal systems, $(\text{CaF}_2)_{1-x}(\text{LaF}_3)_x$, $(\text{BaF}_2)_{1-x}(\text{LaF}_3)_x$, and $(\text{SrF}_2)_{1-x}(\text{LaF}_3)_x$, are given in Fig. 1. X-ray 2θ scans are taken from 20° to 60° for these mixed crystal powders. Typically, four or five Bragg peaks are observed in this region. The 2θ positions are analyzed according to the regular fluorite structure and no additional peaks have been observed, which indicates that the fluorite structure is well preserved and that there is no phase separation even at high LaF₃ concentrations. The lattice constant is calculated with the help of the following formula:

$$a = \frac{\lambda}{2 \sin \theta} \sqrt{h^2 + k^2 + l^2}, \quad (1)$$

where $\lambda = 1.540562 \text{ \AA}$ is the wavelength of the Cu K α line and (h, k, l) are the Miller indices. The lattice constant values calculated from different Bragg peaks are averaged to give the final lattice constant used in Fig. 1(a). The lattice constants we have obtained for the pure CaF₂, BaF₂, and SrF₂ crystals agree exactly with the literature data.³² From the LaF₃ concentration dependence of $\Delta a/a$, it is clear that with the addition of LaF₃, $(\text{CaF}_2)_{1-x}(\text{LaF}_3)_x$, and $(\text{SrF}_2)_{1-x}(\text{LaF}_3)_x$ undergo lattice expansion while $(\text{BaF}_2)_{1-x}(\text{LaF}_3)_x$ undergoes contraction. This finding is consistent with the LaF₃ concentration dependence of the shift of the Raman-active T_{2g} phonon in these three systems.

The results of the density measurements for the three LaF₃-doped mixed crystal systems, $(\text{CaF}_2)_{1-x}(\text{LaF}_3)_x$, $(\text{SrF}_2)_{1-x}(\text{LaF}_3)_x$, and $(\text{BaF}_2)_{1-x}(\text{LaF}_3)_x$ are shown in Fig. 1(b). The calculated densities for the pure CaF₂, BaF₂, and SrF₂ crystals agree precisely with the literature data. The reason that both $\Delta a/a$ and $\Delta\rho/\rho$ display a nonlinear LaF₃ concentration dependence is because these fluorite mixed crystals are interstitial systems,³² i.e., to maintain charge neutrality an interstitial F⁻ ion is produced for each La³⁺ ion introduced.

B. Influence of disorder on the T_{2g} phonon mode

For disordered materials, the k -vector selection rule used for crystalline materials no longer holds. Using the results of Shuker and Gammon describing the low-frequency Raman scattering from vibrational states³³ in glasses, the Raman Stokes (anti-Stokes) intensity from phonons should be proportional to the phonon density of states, $g_{\text{ph}}(\omega)$ and a light-phonon coupling coefficient, C_{ph} . The result is a temperature-dependent Raman Stokes intensity of the form given below:

$$I_{\text{ph}}^S(\omega, T) = [n(\omega, T) + 1] \left\{ g_{\text{ph}}(\omega) \frac{C_{\text{ph}}}{\omega} \right\}, \quad (2)$$

where $n = (e^{\hbar\omega/k_B T} - 1)^{-1}$ is the Bose-Einstein thermal factor. For the Raman anti-Stokes intensity, one simply replaces the $[n(\omega, T) + 1]$ factor in Eq. (2) by $n(\omega, T)$. Note that because of the local field correction $C_{\text{ph}} = c_{\text{ph}} [(\epsilon + 2)/3]^4 = c_{\text{ph}} L$, where ϵ is the optical dielectric constant and L the local field correction factor.

The low-temperature polarized Raman spectra of $(\text{CaF}_2)_{1-x}(\text{LaF}_3)_x$ are shown in Fig. 2 for the whole spectral region ($5\text{--}715 \text{ cm}^{-1}$) examined. For the case of the pure crystal there should be only one Raman-active T_{2g} phonon mode observed in first order;³⁴ however, due to various depolarization effects, such as finite collection angle, imperfect sample alignment, and strain in the cryostat windows, a few percent of the strong T_{2g} signal leaks into other scattering symmetries, as illustrated in the inset of Fig. 2(b). With the addition of LaF₃, defect-induced Raman scattering appears in all scattering symmetries and it increases with increasing

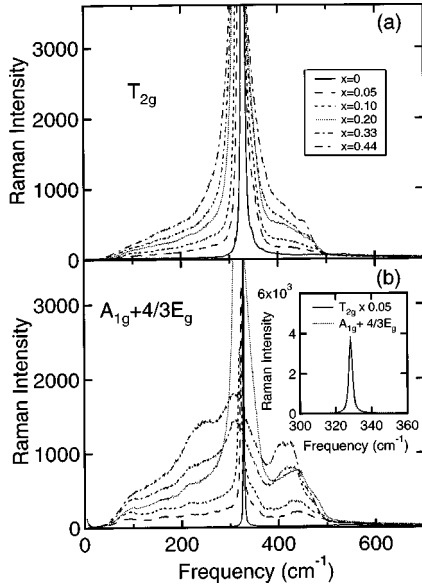


FIG. 2. Polarized Raman spectra of $(\text{CaF}_2)_{1-x}(\text{LaF}_3)_x$ at 1.4 K for six different doping levels. (a) T_{2g} spectra and (b) $A_{1g} + 4/3E_g$ spectra. The inset shows that about 5% of the strong T_{2g} mode leaks into the $A_{1g} + 4/3E_g$ spectra. (Note that the T_{2g} mode is resolution limited at 1.4 K.) The resolution is 2.1 cm^{-1} .

x . Also the main T_{2g} phonon peak broadens and shifts to lower frequencies. The other two mixed crystal systems show similar behavior with the main T_{2g} phonon peak shifting to lower frequencies for $(\text{SrF}_2)_{1-x}(\text{LaF}_3)_x$ but shifting to higher frequencies for $(\text{BaF}_2)_{1-x}(\text{LaF}_3)_x$. These results are consistent with single mode behavior of mixed crystals³⁵ for the lattice constant changes presented in Fig. 1(a).

The low-temperature Raman spectra of the T_{2g} phonon in the $(\text{CaF}_2)_{1-x}(\text{LaF}_3)_x$ mixed crystal systems are shown in Fig. 3. The T_{2g} phonon peak broadens and shifts to lower frequencies monotonically as the LaF_3 concentration increases. Similar broadening behavior is observed for the

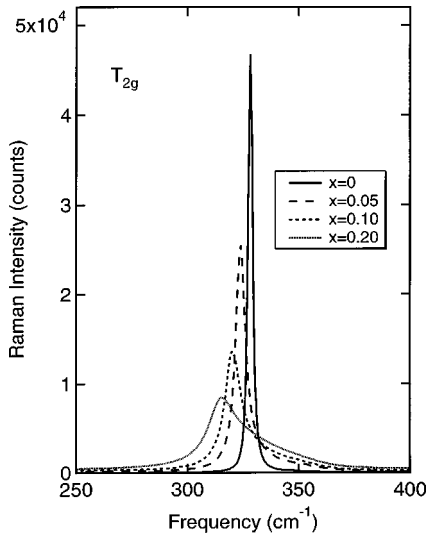


FIG. 3. The Raman-active T_{2g} phonon in $(\text{CaF}_2)_{1-x}(\text{LaF}_3)_x$ at 1.4 K for four different doping levels. The resolution is 2.1 cm^{-1} .

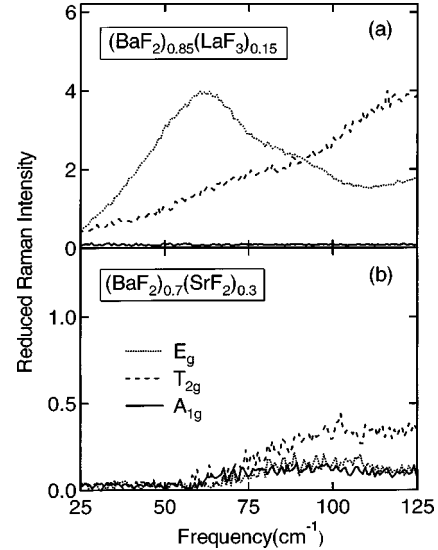


FIG. 4. Reduced Raman spectra in the boson peak region at 1.4 K for different scattering symmetries. (a) $(\text{BaF}_2)_{0.85}(\text{LaF}_3)_{0.15}$ mixed crystal and (b) $(\text{BaF}_2)_{0.7}(\text{SrF}_2)_{0.30}$ mixed crystal.

other two mixed crystal systems $(\text{BaF}_2)_{1-x}(\text{LaF}_3)_x$ and $(\text{SrF}_2)_{1-x}(\text{LaF}_3)_x$, where the LaF_3 concentration dependence also has been systematically studied over the entire range. We have found that the T_{2g} phonon line shape of these LaF_3 -doped fluorite mixed crystals at 1.4 K is remarkably similar to the defect-induced line shape previously measured for pure fluorite crystals at high temperatures ($\sim 800 \text{ K}$) as described in Ref. 4. This comparison provides direct evidence that there could be a connection between the disorder measured at high temperature and the frozen in disorder examined at low temperature. The importance of this observation will become apparent in Sec. IV when an “effective” disorder temperature for these LaF_3 -doped fluorite mixed crystals is identified.

C. Boson peaks and impurity-induced Raman scattering

In the acoustic region, below the TA zone boundary phonon mode frequency, a universal glass feature, namely, the boson peak, has been reported in this type of mixed crystal.^{24,25} Our systematic Raman study of the boson peak for the crystals listed in Table I shows that this feature only appears in E_g symmetry. To bring out this spectral feature it is customary to use the “reduced” Raman intensity, defined as

$$I^{\text{red}}(\omega, T) = \frac{I(\omega, T)}{[n(\omega, T) + 1]\omega}, \quad (3)$$

where $n(\omega, T)$ is the Bose–Einstein thermal factor.

Figure 4(a) shows the three symmetry types observed in Raman scattering for $(\text{BaF}_2)_{0.85}(\text{LaF}_3)_{0.15}$. These results are characteristic of all such La^{3+} -doped mixed crystal samples. A peak is observed only in E_g and the scattering strengths in this frequency region have the following trend: $E_g > T_{2g} > A_{1g}$. Figure 4(b) shows the Raman spectra for a simple

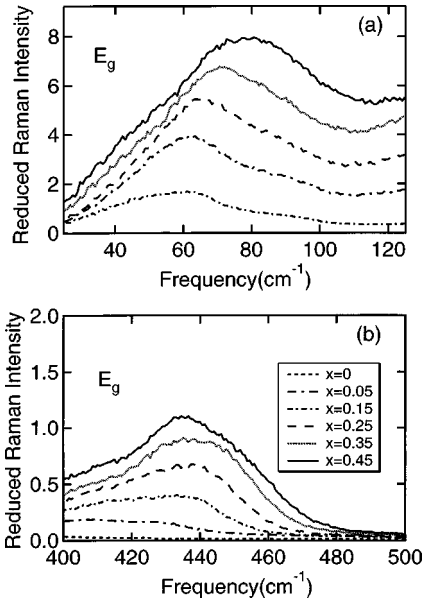


FIG. 5. LaF_3 concentration dependence of the reduced Raman intensity of the Boson peak and an impurity-induced Raman resonant mode in the E_g spectra of $(\text{BaF}_2)_{1-x}(\text{LaF}_3)_x$ at 1.4 K. (a) The boson peak region (note the $x=0$ curve coincides with the horizontal axis) and (b) the impurity induced Raman resonant mode.

mixed crystal system $(\text{BaF}_2)_{0.70}(\text{SrF}_2)_{0.30}$, with isoelectronic substitution. Now a weak maximum at $\sim 90 \text{ cm}^{-1}$ can be seen in both E_g and A_{1g} symmetry types but here the T_{2g} symmetry scattering is the strongest.

The reduced E_g Raman spectra for the $(\text{BaF}_2)_{1-x}(\text{LaF}_3)_x$ mixed crystal system showing the boson peak region versus x are presented in Fig. 5(a). (The $x=0$ trace is on the abscissa.) The corresponding reduced E_g Raman spectra versus x for a high-frequency defect-induced Raman resonant mode are shown in Fig. 5(b). These two E_g spectral features are correlated in the sense that the reduced Raman intensities of both bands increase with increasing LaF_3 concentration in a similar manner. The center frequencies also appear to be correlated with the main T_{2g} phonon peak, which shifts to higher frequencies for $(\text{BaF}_2)_{1-x}(\text{LaF}_3)_x$, but as we shall see that this is not a general effect.

Figure 6 shows the frequency shift of the boson peak versus x for all three mixed crystal systems. A distinguishing property is that the peak frequency ω_{BP} increases with increasing LaF_3 concentration for all three systems even though the T_{2g} phonon peak decreases for the $(\text{CaF}_2)_{1-x}(\text{LaF}_3)_x$, and $(\text{SrF}_2)_{1-x}(\text{LaF}_3)_x$ mixed crystal systems but increases for $(\text{BaF}_2)_{1-x}(\text{LaF}_3)_x$. In contrast the high-frequency resonant mode position [see Fig. 5(b)] has the standard behavior, i.e., versus concentration it follows the corresponding T_{2g} phonon frequency in all three mixed crystal systems. (See Chap. IX of Ref. 35 for a description of the single mode behavior of these mixed crystals.)

Another specific experimental test of the random force constant models comes from our low-frequency Raman results obtained for $(\text{BaSrF}_2)_{0.95}(\text{LaF}_3)_{0.05}$. The boson peak (BP) is observed at 62 cm^{-1} . Within the experimental uncertainty this frequency agrees with Vegard's

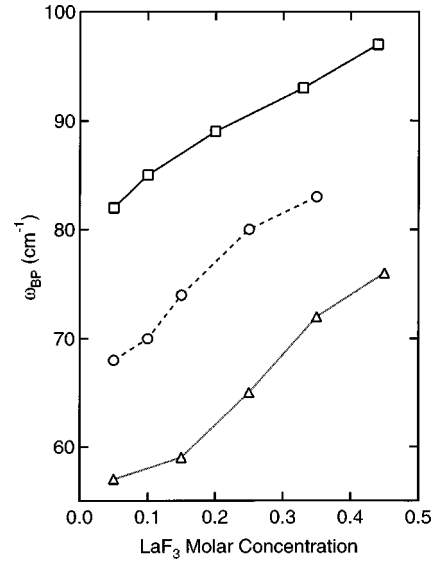


FIG. 6. Boson peak frequency versus dopant concentration: squares for $(\text{CaF}_2)_{1-x}(\text{LaF}_3)_x$, circles for $(\text{SrF}_2)_{1-x}(\text{LaF}_3)_x$, and triangles for $(\text{BaF}_2)_{1-x}(\text{LaF}_3)_x$. For all three lattice systems the boson peak frequency increases with dopant concentration, even though the lattice constant decreases for BaF_2 and increases for the other two.

law^{35,36} if $(\text{BaF}_2)_{0.95}(\text{LaF}_3)_{0.05}$ ($\text{BP}=57 \text{ cm}^{-1}$) and $(\text{SrF}_2)_{0.95}(\text{LaF}_3)_{0.05}$ ($\text{BP}=68 \text{ cm}^{-1}$) are assumed to be the two end points. Clearly the lattice disorder is larger for the BaSrF_2 crystal than for either of the two end points and hence the frequency should have been substantially smaller than the Vegard law prediction according to the random force constant models.^{30,31}

D. Raman scattering in the low-frequency TLS region

It is possible to identify the Raman-active TLS spectrum because its temperature dependence is quite different from that associated with defect-induced scattering in the vibrational spectrum. The temperature dependence of the Stokes Raman intensity due to TLS for splitting $\hbar\omega$ is given by³⁷

$$I_{\text{TLS}}^S(\omega, T) \propto [n(\omega, T) + 1] \tanh\left(\frac{\hbar\omega}{2k_B T}\right) = \frac{1}{1 + \exp(-\hbar\omega/k_B T)} = n_{\text{TLS}}^S(\omega, T), \quad (4)$$

where $n_{\text{TLS}}^S(\omega, T)$ is the ground-state population factor of TLS (excited state population number $n_{\text{TLS}}^A = 1 - n_{\text{TLS}}^S$) and $\omega > 0$ for Stokes and $\omega < 0$ for anti-Stokes Raman scattering. The population fractions $n_{\text{TLS}}^S(\omega, T)$ and $n_{\text{TLS}}^A(\omega, T)$ are determined by Boltzmann distribution. In analogy with the Raman scattering from the vibrational states³³ given in Eq. (2), the Raman Stokes (anti-Stokes) intensity from TLS should be proportional to the density of states of TLS, $g_{\text{TLS}}(\omega)$, a light-TLS coupling coefficient, C_{TLS} (where again $C_{\text{TLS}} = c_{\text{TLS}}L$) and the temperature-dependent factor given in Eq. (4). The result is a temperature-dependent Raman scattering

intensity of the form given below, where $j = S$ or A stands for Stokes or anti-Stokes, respectively,

$$I_{\text{TLS}}^j(\omega, T) = [n_{\text{TLS}}^j(\omega, T)] \left\{ g_{\text{TLS}}(\omega) \frac{C_{\text{TLS}}}{\omega} \right\}. \quad (5)$$

Since the only temperature-dependent quantity on the right-hand side of Eq. (5) is the TLS population numbers n_{TLS}^j , the Raman Stokes and anti-Stokes intensities should be proportional to population numbers as a function of temperature. As temperature increases, n_{TLS}^S decreases from 1 to 0.5 and n_{TLS}^A increases from 0 to 0.5; hence the resonant interaction with TLS decreases with increasing temperature on the Stokes side and increases on the anti-Stokes side. This is the characteristic temperature dependence of Raman scattering from TLS. At higher temperatures, relaxational processes come into play and eventually become the dominant factor as discussed in Ref. 26. For the present work, the focus is the low-temperature region ($T < 20$ K) where the Raman scattering due to relaxational processes can be neglected.

At the lowest frequencies, Raman scattering from TLS is observed, but only for one symmetry type. For the perfect fluorite crystal there is one strongly allowed Raman mode in T_{2g} symmetry but no first-order scattering allowed in A_{1g} and E_g symmetries. With the addition of LaF_3 only low-frequency A_{1g} Raman scattering is observed at low temperatures. In the frequency region below 20 cm^{-1} the Raman intensities in the two other symmetries E_g and T_{2g} are found to be about a factor of ~ 100 weaker than A_{1g} intensity. We suspect that these very weak contributions are probably produced by systematic errors caused by depolarization effects produced by (1) the finite collection angle, (2) imperfect sample alignments, and (3) strains in the cryostat windows.

The low-temperature A_{1g} Raman spectra of LaF_3 -doped $(\text{BaF}_2)_{1-x}(\text{LaF}_3)_x$ fluorite mixed crystals at 1.4 K are displayed in Fig. 7. Six $(\text{BaF}_2)_{1-x}(\text{LaF}_3)_x$ samples with $x = 0, 0.05, 0.15, 0.25, 0.35,$ and 0.45 are shown. Both the Stokes and anti-Stokes sides are displayed. To ensure that the elastic Rayleigh scattering does not influence the Raman spectra of the mixed crystals, a lower limit of 5 cm^{-1} is used and as a result asymmetric spectra are obtained for the Stokes and anti-Stokes region at low frequencies. On the Stokes side, the Raman intensity increases with increasing lanthanum concentration, while on the anti-Stokes side no Raman signal is observed at 1.4 K for any of the six fluorite mixed crystals. These asymmetric spectra demonstrate that elastic Rayleigh scattering plays no significant role in our measurements, because it would enter into both the Stokes and anti-Stokes spectra with equal strength. Another reason for examining the anti-Stokes spectra is to make sure that there is no background due to thermal luminescence. None is observed here. Similar properties are found in all the mixed crystal samples measured in this work.

The temperature dependence of the Raman A_{1g} spectra from 1.4 to 20.0 K of four LaF_3 -doped fluorite mixed crystals representing the four fluorite systems, $(\text{CaF}_2)_{1-x}(\text{LaF}_3)_x$, $(\text{SrF}_2)_{1-x}(\text{LaF}_3)_x$, $(\text{BaF}_2)_{1-x}(\text{LaF}_3)_x$,

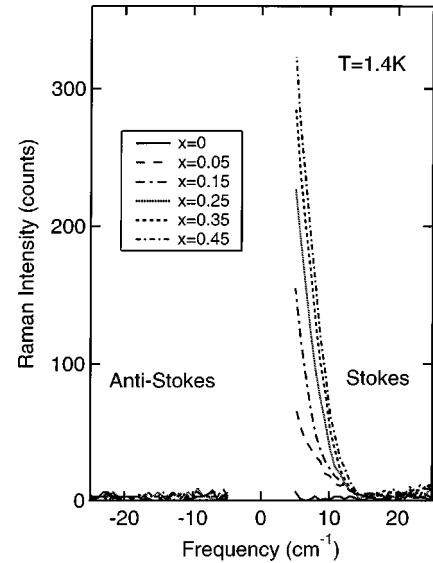


FIG. 7. Low-frequency Raman A_{1g} spectra of $(\text{BaF}_2)_{1-x}(\text{LaF}_3)_x$ mixed crystal system at 1.4 K. Both Stokes and anti-Stokes spectra are shown. The resolution is 2.1 cm^{-1} .

and $(\text{BaSrF}_2)_{1-x}(\text{LaF}_3)_x$, are displayed in Figs. 8(a), 8(b), 8(c), and 8(d). The data for $(\text{CaF}_2)_{0.67}(\text{LaF}_3)_{0.33}$ is shown in Fig. 8(a), for $(\text{SrF}_2)_{0.65}(\text{LaF}_3)_{0.35}$, in Fig. 8(b), for $(\text{BaF}_2)_{0.55}(\text{LaF}_3)_{0.45}$, in Fig. 8(c), and for $(\text{BaSrF}_2)_{0.95}(\text{LaF}_3)_{0.05}$, in Fig. 8(d). The low-frequency A_{1g} spectra of both the Stokes and anti-Stokes sides are displayed to extract the maximum amount of information from the temperature-dependent spectra. From 1.4 to 20 K, the Raman intensities for all four fluorite mixed crystals decrease with increasing temperature on the Stokes side and increase with increasing temperature on the anti-Stokes side. This charac-

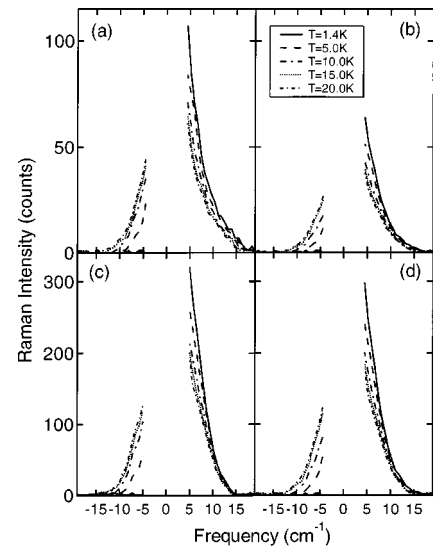


FIG. 8. Temperature dependence of the low-frequency Raman A_{1g} spectrum for different mixed crystal systems from 1.4 to 20 K. Both Stokes and anti-Stokes spectra are shown. The resolution is 2.1 cm^{-1} . (a) $(\text{CaF}_2)_{0.67}(\text{LaF}_3)_{0.33}$, (b) $(\text{SrF}_2)_{0.65}(\text{LaF}_3)_{0.35}$, (c) $(\text{BaF}_2)_{0.55}(\text{LaF}_3)_{0.45}$, and (d) $(\text{BaSrF}_2)_{0.95}(\text{LaF}_3)_{0.05}$.

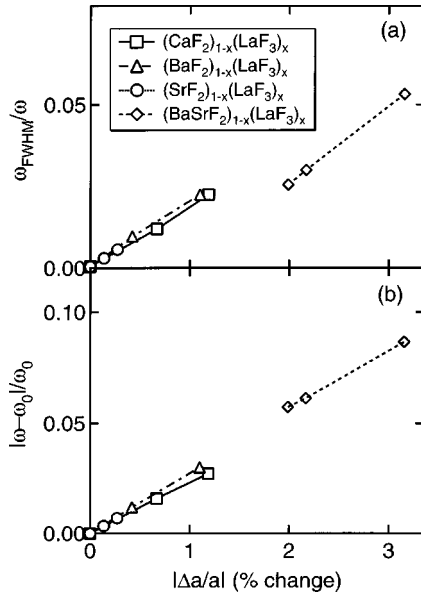


FIG. 9. The behavior of the shift and linewidth of the T_{2g} phonon as a function of the lattice strain $|\Delta a/a|$ in four LaF_3 -doped mixed crystal systems at low dopant concentrations. (a) $\omega_{\text{FWHM}}/\omega$ versus $|\Delta a/a|$ and (b) $|\omega - \omega_0|/\omega_0$ versus $|\Delta a/a|$.

teristic temperature dependence of Raman scattering from TLS is observed for all the fluorite mixed crystals studied.

IV. DATA ANALYSIS AND DISCUSSION

A. T_{2g} phonons and the lattice strain $\Delta a/a$

The LaF_3 concentration dependence of both the T_{2g} phonon and the lattice strain $|\Delta a/a|$ show similar trends as seen in Figs. 1(a) and 3. To explore this connection further, the full width half-maximum (FWHM) and frequency shift of the T_{2g} phonon versus the lattice strain are plotted in Fig. 9. Figures 9(a) and 9(b) demonstrate that both the shift and half-width of the T_{2g} phonon depend linearly on the lattice strain $|\Delta a/a|$ at low LaF_3 concentrations. These properties are well described by optical strain broadening theory,^{38,39} which leads to a Lorentzian-shaped phonon line whose frequency shift and half-width are proportional to ρA and $\rho|A|$, respectively. The connection between ρA and $\Delta a/a$, the fractional lattice parameter change, is

$$\frac{\Delta a}{a} = 4\pi \left\{ \frac{1 - \sigma}{1 + \sigma} \right\} \rho A, \quad (6)$$

where A is the ‘‘elastic strength’’ of the impurity, σ is Poisson’s ratio, and ρ is the density of the strain sources. Thus both the frequency shift and half-width vary linearly with $\Delta a/a$. The factors of proportionality depend on the strain coupling parameters of the particular defect-lattice system being studied.⁴⁰

B. Raman scattering from TLS

The parameters associated with the temperature dependence of Raman scattering from the resonant interaction with TLS at low frequencies can be examined in some detail us-

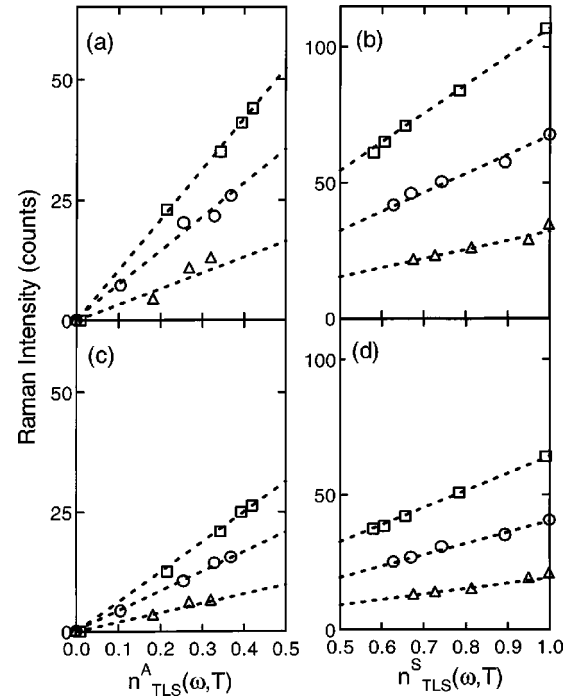


FIG. 10. Temperature dependence of the low-frequency Raman A_{1g} spectra from 1.4 to 20 K as a function of TLS population factor for different mixed crystal systems. (a) $(\text{CaF}_2)_{0.67}(\text{LaF}_3)_{0.33}$ Raman anti-Stokes intensity versus n_{TLS}^A , (b) $(\text{CaF}_2)_{0.67}(\text{LaF}_3)_{0.33}$ Raman Stokes intensity versus n_{TLS}^S , (c) $(\text{SrF}_2)_{0.65}(\text{LaF}_3)_{0.35}$ Raman anti-Stokes intensity versus n_{TLS}^A , and (d) $(\text{SrF}_2)_{0.65}(\text{LaF}_3)_{0.35}$ Raman Stokes intensity versus n_{TLS}^S .

ing Eq. (5). Since the only temperature-dependent quantity on the right-hand side of Eq. (5) is the TLS population numbers n_{TLS}^i , then by plotting the Raman intensity data versus the population number n_{TLS}^i for either Stokes or anti-Stokes scattering, a linear dependence becomes the characteristic feature of the TLS spectroscopic measurement.

The observed linear dependence of the Raman TLS scattering versus population of the appropriate state is demonstrated experimentally in Figs. 10 and 11. The temperature dependence of the Raman A_{1g} anti-Stokes intensity for a $(\text{CaF}_2)_{0.67}(\text{LaF}_3)_{0.33}$ mixed crystal is shown from 1.4 to 20 K in Fig. 10(a); for a $(\text{SrF}_2)_{0.65}(\text{LaF}_3)_{0.35}$ in Fig. 10(c); for a $(\text{BaF}_2)_{0.55}(\text{LaF}_3)_{0.45}$ in Fig. 11(a), and for a $(\text{BaSrF}_2)_{0.95}(\text{LaF}_3)_{0.05}$ in Fig. 11(c). The corresponding dependencies of the Raman Stokes intensity on n_{TLS}^S are plotted in Figs. 9(b), 9(d), 10(b), and 10(d). Clearly both measured Raman anti-Stokes and Stokes intensities depend linearly on n_{TLS}^i for the four crystals shown. Because both the temperatures and the frequencies are measured, only the slope in each data set is an experimental free parameter to be determined. Behavior similar to that shown here is found for all the fluorite mixed crystals listed in Table I. An important advantage of the Raman technique is that both Stokes and anti-Stokes scattering can be examined separately so that the slope is over determined when fitting the experimental data to Eq. (5). The same slope is found using the Stokes or the anti-Stokes data for a particular mixed crystal. The end result is that the low-frequency A_{1g} Raman spectrum in fluorite

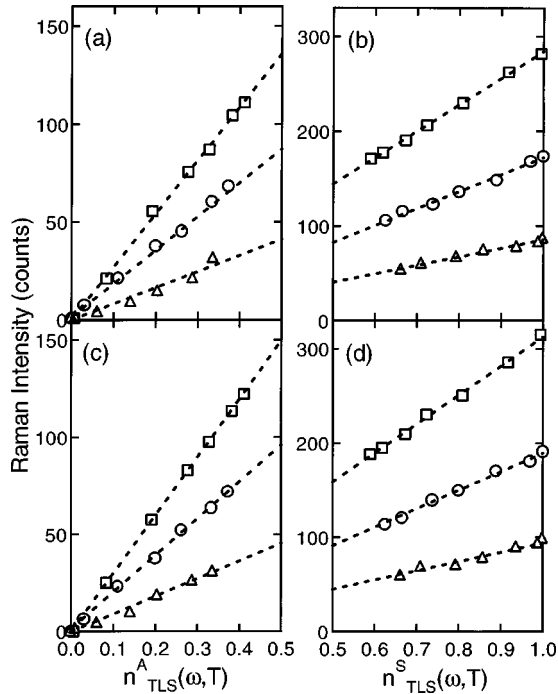


FIG. 11. Temperature dependence of the low-frequency Raman A_{1g} spectra from 1.4 to 20 K as a function of TLS population factor for different mixed crystal systems. (a) $(\text{BaF}_2)_{0.55}(\text{LaF}_3)_{0.45}$ Raman anti-Stokes intensity versus n_{TLS}^A , (b) $(\text{BaF}_2)_{0.55}(\text{LaF}_3)_{0.45}$ Raman Stokes intensity versus n_{TLS}^S , (c) $(\text{BaSrF}_2)_{0.95}(\text{LaF}_3)_{0.05}$ Raman anti-Stokes intensity versus n_{TLS}^A , and (d) $(\text{BaSrF}_2)_{0.95}(\text{LaF}_3)_{0.05}$ Raman Stokes intensity versus n_{TLS}^S .

mixed crystals can be convincingly identified with scattering from the direct interaction with a broad distribution of TLS.

C. Absence of excited state TLS transitions in Raman scattering

The far-infrared absorption study¹⁸ of these same fluorite crystals has shown both a TLS spectrum extending up to about 20 cm^{-1} and also excited state TLS transitions at higher frequencies, from 20 to 40 cm^{-1} . The identification with excited-state transitions was made possible by the temperature-dependent study over a broad frequency region. As the low-frequency TLS absorption spectrum becomes weaker with increased temperature the absorption coefficient corresponding to higher-frequency excited-state transitions becomes stronger over a restricted frequency region in such a way that the oscillator strength sum rule remained constant. Since this sum rule is quite general and applies to any anharmonic arrangement of levels,⁴¹ including those involving tunneling, the corresponding temperature-induced area changes in the absorption coefficient in the different frequency regions provides a unique signature.

Figure 12 shows the temperature-dependent Raman spectra for (a) $(\text{CaF}_2)_{0.67}(\text{LaF}_3)_{0.33}$, (b) $(\text{SrF}_2)_{0.65}(\text{LaF}_3)_{0.35}$, and (c) $(\text{BaF}_2)_{0.55}(\text{LaF}_3)_{0.45}$ but now plotted as $\omega I(\omega, T)/(n+1)$ so that any Raman-active excited-state population effect would display the same area as the TLS effect. At low frequencies the TLS temperature effect is evident for all

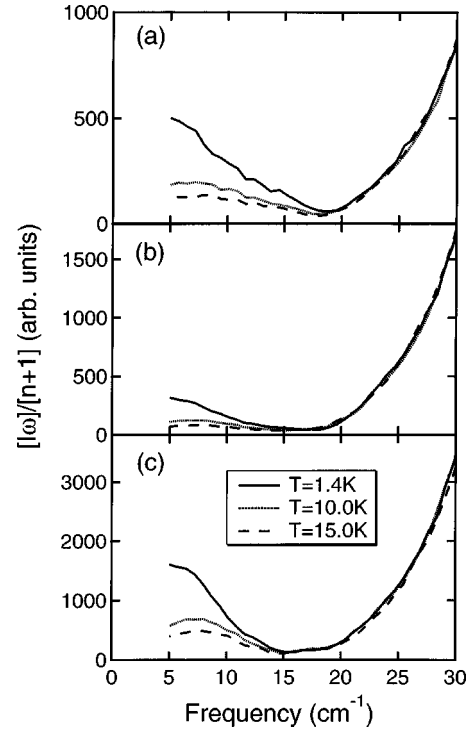


FIG. 12. Temperature-dependent examination of normalized Raman intensity in the TLS frequency region for three different mixed crystals. (a) $(\text{CaF}_2)_{0.67}(\text{LaF}_3)_{0.33}$, (b) $(\text{SrF}_2)_{0.65}(\text{LaF}_3)_{0.35}$, and (c) $(\text{BaF}_2)_{0.55}(\text{LaF}_3)_{0.45}$. This presentation of the scattering data demonstrates that there are no Raman-active TLS excited-state transitions.

three systems. However, in the frequency region 20 to 30 cm^{-1} no change in the spectrum is observed over this important temperature range. This temperature-independent behavior at these higher frequencies is consistent with that expected for defect-induced Raman scattering from harmonic excitations. These results indicate that TLS excited states in these mixed crystals, while IR active, are not Raman active.

D. Boson peak and its correlation with a defect-induced Raman band

In analyzing the boson peak data it is helpful to start from the low concentration end. For the three host crystals $\text{CaF}_2:\text{SrF}_2:\text{BaF}_2$ the BP band centers $82:68:57 \text{ cm}^{-1}$ appear below the lowest TA frequency at the L point $146:100:66 \text{ cm}^{-1}$. [Note that these L point values are for room temperature and hence they would be a bit ($\sim 10\%$) larger at 1.4 K.] These BP frequencies should be compared with the earlier low-temperature Raman results³ for $(\text{SrF}_2)_{0.995}(\text{EuF}_2)_{0.005}$ and $(\text{BaF}_2)_{0.995}(\text{EuF}_2)_{0.005}$ since the mass and ionic radius of both defects are very similar. The former crystal has an E_g impurity-induced resonance at 83 cm^{-1} while the latter has one at 70 cm^{-1} . Since both resonant and localized defect modes typically stem from zone boundary frequencies, the appearance of resonances in the vicinity of the TA frequency at the L point associated with heavy defect ions such as La^{3+} and Eu^{2+} is not surprising.³⁵ However, it should be noted

that for cubic lattice models with only nearest-neighbor force constant changes and a heavy impurity ion the E_g resonance drops out of the La branch.⁴²

The unusual property of the BP E_g feature in the La mixed crystals is the observation that the frequency increases with molar concentration (see Fig. 6) independent of whether this LaF_3 doping causes the average lattice constant to increase or decrease as shown in Fig. 1. Earlier studies⁴³ on low-frequency resonances in mixed ionic crystals have shown that the resonant frequency increases or decreases according to Vegard's law. Disorder is one obvious property that does increase with increased LaF_3 concentration.

The dynamical features associated with lattice disorder have been studied numerically over many years. Of particular interest for our experiments is the work of Payton and Visscher⁴⁴ who calculated the density of vibrational modes for a three-dimensional (3D) diatomic lattice. The model consisted of $6 \times 6 \times 40$ particles (NaCl structure) connected by central and noncentral nearest-neighbor force constants. The disorder is introduced by randomly choosing the value for the force constant within a specified range. They found that with increasing disorder the peaks in the distribution moved to lower frequencies. More recent numerical studies,^{30,31} which have focused explicitly on the origin of the boson peak in systems with lattice disorder, confirm these early results in that increased disorder lowers the density of modes. In addition, Ref. 31 proposes that with increasing disorder the BP drops out of the lowest van Hove singularity, which for our mixed crystal system would be the TA frequency at the L point.

In comparing our experimental results with the lattice disorder models the BP for the LaF_3 -doped fluorite mixed crystals is indeed at frequencies lower than the TA frequency at the L point, but the fact that the frequency increases with increasing disorder does not agree with any of these models. Particularly interesting from this perspective are the low-temperature experimental Raman results for $(\text{BaF}_2)_{0.70}(\text{SrF}_2)_{0.30}$, which show the development of a weak BP for both A_{1g} and E_g symmetries centered at about 90 cm^{-1} , a frequency much larger than the BaF_2 TA frequency at the L point.

A different kind of comparison of lattice disorder comes from the $(\text{BaF}_2)_{0.95}(\text{LaF}_3)_{0.05}$, $(\text{BaSrF}_2)_{0.95}(\text{LaF}_3)_{0.05}$, and $(\text{SrF}_2)_{0.95}(\text{LaF}_3)_{0.05}$ series. Here the disorder in the middle system is much larger than for either pure host yet the BP frequency of this mixed crystal still agrees with Vegard's law prediction in which the effective lattice constant and hence frequency only depends on the relative concentration and the lattice constants at the two end points.³⁵ If lattice disorder was the controlling factor in determining the frequency position of the BP then for the BaSrF_2 mixed crystal case it should have appeared at a frequency much smaller than predicted by the virtual crystal model.

Another property that does increase with increasing LaF_3 concentration for all three host crystals is the density. If the increased density is associated with a resonant mode excitation then its frequency would decrease. If the increased density is associated with an increase in the average crystal mass and not with the excitation then again for a resonant mode

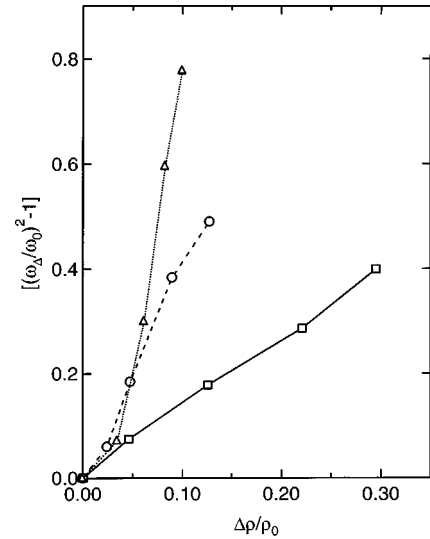


FIG. 13. Boson peak frequency shift versus crystal density change. The initial (ρ_0, ω_0) values are taken at the $x=0.05$ mole fraction point. For each host the frequency (from Fig. 6) increases with increasing density, opposite to the shift predicted for a resonant mode with a mass increase in the host lattice.

the frequency still decreases.⁴⁵ [See Eq. (6.15) in Ref. 35.] Figure 13 presents plots of the BP frequency shifts versus the density change, i.e.,

$$\left(\frac{\omega_{\Delta}^2}{\omega_0^2} - 1 \right) \text{ versus } \left(\frac{\Delta\rho}{\rho_0} \right)$$

for the three mixed crystal systems. The starting density ρ_0 is for $x=0.05$. Clearly the frequency shift is correlated with the density even though the effect has the opposite sign from that expected for a defect resonance. The BP responds like it has a negative mass. We conclude that the BP must be another feature of the disorder and not simply a defect mode.

Our Raman scattering experiments demonstrate that there is a direct proportionality between the strength in the boson peak region and that in the high-frequency defect-induced resonant mode region. At the same time we find no such proportionality between the scattering strength in the boson peak region and that in the TLS region for different host systems. These findings are quantified by means of the two comparisons shown in Fig. 14. In Fig. 14(a) the integrated intensity of the TLS region is graphed versus the integrated intensity of the high-frequency defect-induced resonant band [see, e.g., Fig. 5(b)] as a function of LaF_3 concentration for the three mixed crystal systems. No direct proportionality is observed and the TLS intensity tends to saturate at high doping levels, which is particularly obvious for the CaF_2 series. In Fig. 14(b) the integrated intensity of the boson peak region is graphed versus the same abscissa. The linear dependence between the integrated intensity in the boson peak region and the integrated intensity in the higher-frequency defect-induced E_g band for the different LaF_3 concentrations is apparent. These two Raman spectral features are indeed correlated to each other and the results suggest that they have a common origin. The lack of such a correlation between the

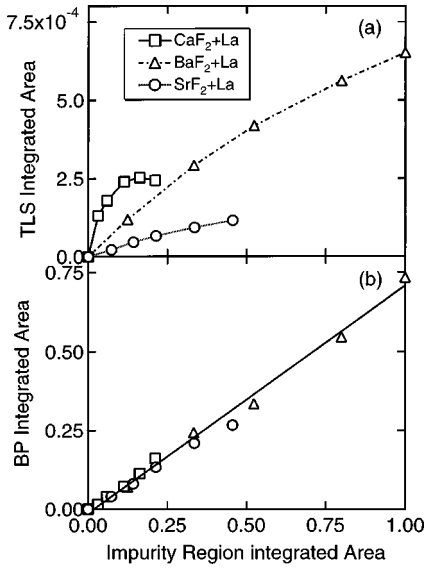


FIG. 14. Comparison of the integrated intensity in the TLS region and in the boson peak region with the integrated intensity of a defect induced E_g band in the LO region for three mixed crystal systems at 1.4 K. (a) The integrated intensity in the TLS region versus the integrated intensity in a defect induced Raman band in the LO region, and (b) the integrated intensity in the boson peak region versus the integrated intensity in a defect induced Raman band in the LO region.

Raman scattering from the boson peak and that from the TLS is an important find. Apparently the TLS spectrum and the boson feature do not have a common origin in these fluorite mixed crystals.

E. Separating the number density of Raman-active TLS from the coupling coefficient

An estimate of the number density per unit frequency interval of Raman-active TLS states can be obtained from the data by comparing the ratio between the scattering found for TLS with that found for the first-order T_{2g} phonon scattering from the pure system. This should provide a reasonable estimate since the defect-induced Raman polarizability depends mainly on the surrounding host lattice.^{46,47}

TABLE II. Collection of data on fluorite mixed crystals. Columns 2, 3, and 4: the lattice constants, density, and the Debye temperature θ_D . Column 5: the Raman active optical phonon frequency ω_R . Column 6: the number density of Raman active T_{2g} mode $S_{T_{2g}}$. Column 7: the temperature parameter α used in Eq. (11); columns 8, 9, 10: the fitting parameters z , c , and T_a used in the law of mass action, Eq. (10). Column 11: the effective temperature for the different crystals doped with 5% LaF_3 . Column 12: the dipole moment of TLS as given in the expression for infrared absorption (see Fig. 21).

Host crystal	Lattice constant (Å)	Density ^a (g/cm ³)	θ_D ^a (K)	ω_R ^a (cm ⁻¹)	$S_{T_{2g}}$ (10 ²² /cm ³)	α (10 ⁻⁵ /K)	z (assoc. deg.)	c (× 10 ⁻⁵)	T_a (K)	T_{eff} (5% La) (K)	μ (Debye)
CaF ₂	5.463 ^a	3.18 ^a	519 ^a	321.5 ^a	0.82	4.38	850	5.0	730	221	0.64
SrF ₂	5.800 ^a	4.24 ^a	380 ^a	285.5 ^a	0.68	3.97	700	7.3	680	57	0.74
BaF ₂	6.200 ^a	4.83 ^a	282 ^a	241.0 ^a	0.56	5.91	960	8.9	1100	134	1.54
BaSrF ₂	6.011	4.55		265.2	0.63	4.94	870	6.7	870	983	

^aReference 32.

The first approximation is to set $C_{\text{TLS}} \approx C_{T_{2g}} = \text{constant}$, where $C_{T_{2g}}$ is the light- T_{2g} phonon coupling coefficients of the host material and $(n_{T_{2g}} + 1) = 1$ at $T = 1.4$ K is the appropriate Bose-Einstein thermal factor for T_{2g} phonons. Given that TLS appear to be one-dimensional (1D) objects in 3D crystals this is a reasonable starting point. Setting $C_{\text{TLS}} \approx \text{constant}$ cannot be correct for all frequencies since the observed Raman scattering from TLS only extends over a finite frequency range and since TLS, which are not Raman-active, may occur up to much larger frequencies. By focusing only on the Raman-active $g_{\text{TLS}}(\omega)$ we include the cutoff in its frequency dependence. The appropriate ratio is

$$\frac{\omega(I_{\text{TLS}}^S/n_{\text{TLS}}^S)}{\int d\omega \omega(I_{T_{2g}}^S)} = \frac{g_{\text{TLS}}(\omega)}{\int d\omega g_{T_{2g}}(\omega)} = \frac{g_{\text{TLS}}(\omega)}{S_{T_{2g}}}, \quad (7)$$

where the total number density of T_{2g} phonon modes $S_{T_{2g}}$ is related to the formula unit number density. For fluorite crystals, such as CaF₂, there are three atoms per unit cell, so the number of unit cells per unit volume is equivalent to the number of formula units per unit volume. For three atoms per unit cell, there are nine modes in total, three acoustic and six optic. Among the six optic modes, there are three T_{2g} modes (triply degenerate), one LO and two TO modes that are IR active (T_{1u}). So the number density of T_{2g} phonon modes is equal to 1/3 of the number density of formula units. The values are given in column 6 of Table II. For the $(\text{BaSrF}_2)_{0.95}(\text{LaF}_3)_{0.05}$ and $(\text{BaSrF}_2)_{0.99}(\text{LaF}_3)_{0.01}$ mixed crystals the molar composition of the pure materials are used for the average values.

Since the experimental ratio on the left-hand side of Eq. (7) is known for each sample, as is $S_{T_{2g}}$, the total number density of T_{2g} phonon modes, the value of $g_{\text{TLS}}(\omega)$ can be determined explicitly to be

$$g_{\text{TLS}}(\omega) = S_{T_{2g}} \frac{\omega(I_{\text{TLS}}^S/n_{\text{TLS}}^S)}{\int d\omega \omega(I_{T_{2g}}^S)}. \quad (8)$$

In Figs. 15(a) and 15(b), the density of states per unit frequency range of Raman-active TLS is plotted versus frequency for two $(\text{BaF}_2)_{1-x}(\text{LaF}_3)_x$ crystals. Each of the dot-

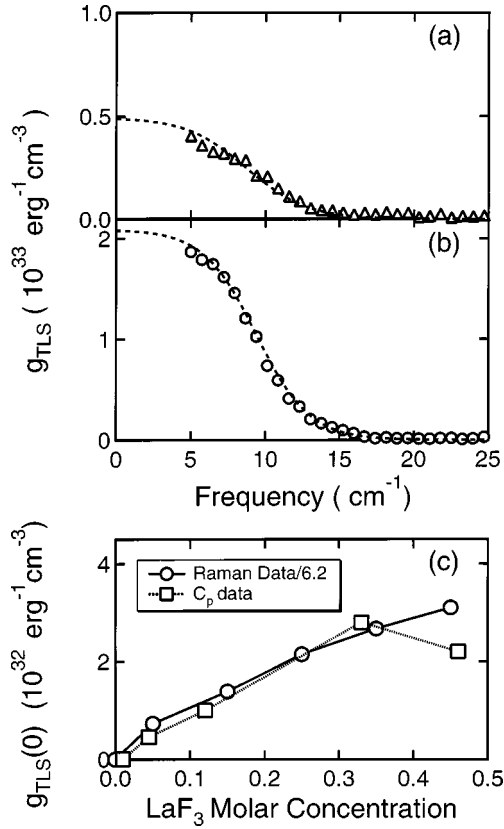


FIG. 15. Comparison of the density of state of TLS derived from Raman scattering with that from specific heat in the $(\text{BaF}_2)_{1-x}(\text{LaF}_3)_x$ mixed crystal system. (a) Frequency dependence of the density of state of TLS from Raman scattering in $(\text{BaF}_2)_{0.55}(\text{LaF}_3)_{0.45}$, (b) frequency dependence of the density of state of TLS from Raman scattering in $(\text{BaF}_2)_{0.95}(\text{LaF}_3)_{0.05}$, and (c) $g_{\text{TLS}}(0)$ values from Raman scattering compared to \bar{P} values from specific heat (Ref. 14) in the $(\text{BaF}_2)_{1-x}(\text{LaF}_3)_x$ mixed crystal system. The dotted curves in (a) and (b) are the least-square fits to the density of states of TLS.

ted curves displayed in Figs. 15(a) and 15(b) represents a least-square fit to $g_{\text{TLS}}(\omega)$ using a three parameter function of the form $g(\omega) = a/\{\exp[b(\omega-d)]+1\}$, where a , b , and d are the fitting parameters. Because of the frequency dependence of $g_{\text{TLS}}(\omega)$, we need to estimate the $g_{\text{TLS}}(0)$ values in order to compare these values with the \bar{P} values (density of states of TLS) derived from the specific-heat measurements. Such a comparison is shown in Fig. 15(c) for $(\text{BaF}_2)_{1-x}(\text{LaF}_3)_x$ crystals. This renormalization is necessary to address some of the limitations associated with the approximation $C_{\text{TLS}} \approx C_{T_{2g}}$. The specific-heat \bar{P} values for these mixed crystals are taken from Ref. 14. The $g_{\text{TLS}}(0)$ and \bar{P} have similar concentration dependence in $(\text{BaF}_2)_{1-x}(\text{LaF}_3)_x$ crystals is illustrated in Fig. 15(c). However, the Raman $g_{\text{TLS}}(0)$ values are a factor of 6.2 larger than the specific-heat \bar{P} values. (Note the local-field correction for the Raman scattering $L=3.75$ accounts for part of this difference.) Since the specific-heat \bar{P} values are determined without any coupling assumptions, the simple Raman

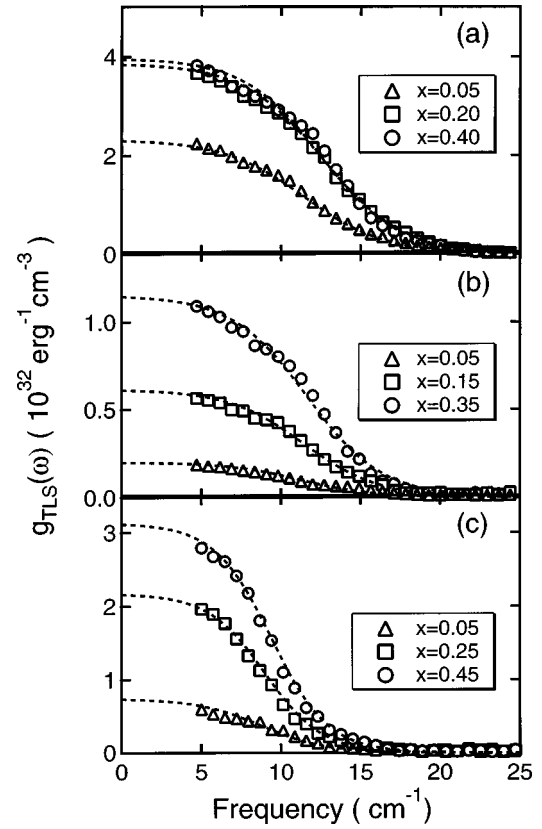


FIG. 16. The frequency dependence of the density of states of TLS in three fluorite mixed crystal systems doped with different molar fractions of LaF_3 at 1.4 K (a) $(\text{CaF}_2)_{1-x}(\text{LaF}_3)_x$, (b) $(\text{SrF}_2)_{1-x}(\text{LaF}_3)_x$, and (c) $(\text{BaF}_2)_{1-x}(\text{LaF}_3)_x$. The dotted curves in (a)–(c) are the least-square fits to the density of states of TLS.

approximation $C_{\text{TLS}} \approx C_{T_{2g}}$ needs to be modified. We now set $C_{\text{TLS}} = 6.2C_{T_{2g}}$ so that the Raman $g_{\text{TLS}}(0)$ values and the specific-heat \bar{P} values agree in $(\text{BaF}_2)_{1-x}(\text{LaF}_3)_x$ crystals. This new relationship between the coupling constants is more robust albeit the frequency dependence in C_{TLS} is neglected. The same correction factor is used for all other mixed crystal systems.

The density of states per unit frequency range of Raman-active TLS is plotted versus frequency for three $(\text{CaF}_2)_{1-x}(\text{LaF}_3)_x$ crystals in Fig. 16(a). Similar behavior is seen in Fig. 16(b) for the $(\text{SrF}_2)_{1-x}(\text{LaF}_3)_x$ system, and in Fig. 16(c) for the $(\text{BaF}_2)_{1-x}(\text{LaF}_3)_x$ system. Since the data are quite smooth the three parameter fit has been used to characterize all of these Raman results. The fit values for the spectral density $g_{\text{TLS}}(0)$ are given in Table I, column 3. An interesting discovery is that although the height of each curve depends on the LaF_3 concentration, the width of the TLS spectrum does not.

Figure 17 presents the fitted Raman density of TLS 1/2 height frequency value d versus the LaF_3 concentration for the three different host crystals. Within the experimental uncertainties of the experiments the TLS spectral width is independent of the LaF_3 concentration, of the crystal density, of whether the lattice has expanded or contracted, and of the increase in the effective disorder.

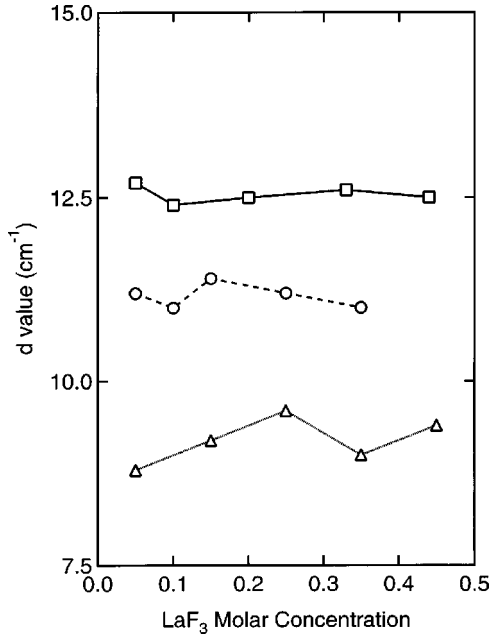


FIG. 17. The Raman-active TLS density of states half-frequency value d versus LaF_3 concentration for the three different hosts. Squares, $(\text{CaF}_2)_{1-x}(\text{LaF}_3)_x$; circles, $(\text{SrF}_2)_{1-x}(\text{LaF}_3)_x$; and triangles, $(\text{BaF}_2)_{1-x}(\text{LaF}_3)_x$. The value depends on the host, however is essentially independent of the LaF_3 concentration and hence the disorder.

F. The total number density of Raman active two-level systems

Because of the existence of a high-frequency cutoff in the Raman active $g_{\text{TLS}}(\omega)$, we can calculate the total number density of Raman-active TLS, S_{TLS} . Since the fits shown in Figs. 16(a), 16(b), and 16(c) are quite good, we use the fitted function of $g_{\text{TLS}}(\omega)$ to calculate S_{TLS} . The integrated area under each curve from 0 to 100 cm^{-1} ,

$$\int d\omega g_{\text{TLS}}(\omega) = S_{\text{TLS}}, \quad (9)$$

provides an estimate of the total number density of Raman-active TLS, S_{TLS} .

Figure 18 presents the measured total number density of Raman-active TLS, S_{TLS} (left ordinate) for the different hosts as a function of LaF_3 molar fraction at 1.4 K. (The dotted line provides an aid to the eye.) Note that for the CaF_2 host S_{TLS} saturates at high LaF_3 molar fraction (>0.2) while the dependence for the other systems is only slightly nonlinear. Also for a given specific LaF_3 molar fraction the S_{TLS} values are quite different for different hosts. Specifically, the S_{TLS} values for the 0.05 molar fraction of $\text{LaF}_3:\text{SrF}_2$ has the smallest value, BaF_2 is somewhat larger, CaF_2 larger still, while the BaSrF_2 mixed crystal has the largest S_{TLS} value of all.

This last observation is a key result since it demonstrates that the number density S_{TLS} depends more generally on the disorder in the lattice, not simply on the molar fraction of LaF_3 alone. The variability of the number density for fixed concentration and the independence of the high-frequency cutoff with concentration are two indicators that these TLS

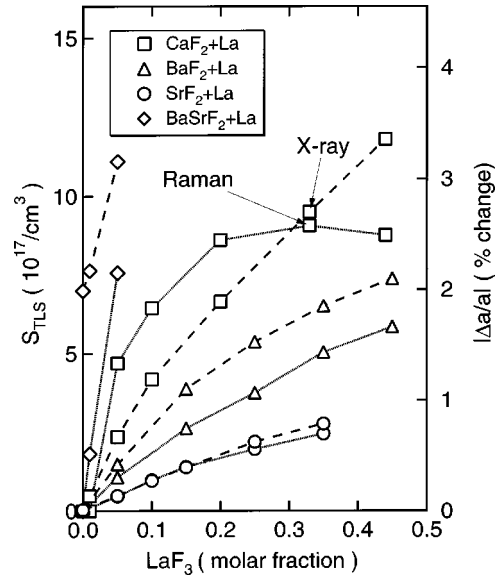


FIG. 18. The dependence of the TLS density S_{TLS} and the lattice strain $|\Delta a/a|$ on LaF_3 molar fraction for three fluorite hosts; a $(\text{BaSrF}_2)_{0.95}(\text{LaF}_3)_{0.05}$, and a $(\text{BaSrF}_2)_{0.99}(\text{LaF}_3)_{0.01}$ mixed crystal.

are not simply the result of strain-induced inhomogeneous broadening of standard defect-induced tunneling levels, a hypothesis that has been used to characterize broad distributions of molecular tunneling states such as CN^- in mixed alkali halide crystals.⁴⁸⁻⁵²

In an attempt to find the connection between S_{TLS} and lattice disorder we focus on the measured $|\Delta a/a|$ as an indicator of lattice strain. We shall use it as a simple measure of the disorder in these fluorite mixed crystal systems over the entire molar fraction range of LaF_3 studied. The x-ray results giving $|\Delta a/a|$ are described by the dashed curves in Fig. 18 (right ordinate) as a function of the LaF_3 molar fraction. The nonlinear dependence of $|\Delta a/a|$ with respect to LaF_3 is a consequence of the interstitial behavior of these fluorite mixed crystals. For LaF_3 -doped SrF_2 , BaF_2 , and the BaSrF_2 mixed crystals there is a fairly good correlation between S_{TLS} and the lattice disorder parameter $|\Delta a/a|$, while for CaF_2 the comparison looks completely different. The end result is that the total number density of TLS S_{TLS} and the lattice disorder parameter $|\Delta a/a|$ exhibit similar concentration dependence with LaF_3 for only three of the four different systems.

It should be emphasized that the S_{TLS} value does not depend on whether the lattice undergoes expansion {as for $(\text{CaF}_2)_{1-x}(\text{LaF}_3)_x$ and $(\text{SrF}_2)_{1-x}(\text{LaF}_3)_x$ } or contraction {as for $(\text{BaF}_2)_{1-x}(\text{LaF}_3)_x$ }. Defect dynamics of tunneling and nontunneling systems have been studied for many years using hydrostatic pressure and the results always show that increased pressure decreases the likelihood of tunneling.^{53,54} From that point of view one would expect that the BaF_2 system would show a decrease in the total number density with decreasing lattice constant while the other two hosts would show an increase of S_{TLS} with increasing lattice constant. However, this is not what is observed experimentally. The fact that S_{TLS} depends on the magnitude of the strain demonstrates that strain inhomogeneity, which is directly re-

lated to the strain magnitude but not its sign, is the key parameter rather than a uniform hydrostatic strain.

G. Frozen in disorder and the law of mass action

From these measurements there are four unusual experimental signatures that stand out. (1) The S_{TLS} value is many orders of magnitude smaller than the nominal La-defect concentration. (2) As a function of the lattice disorder parameter $|\Delta a/a|$, S_{TLS} saturates for the $(\text{CaF}_2)_{1-x}(\text{LaF}_3)_x$ mixed crystals. (3) For CaF_2 , SrF_2 and BaF_2 crystals doped with ≤ 0.01 molar fraction of LaF_3 , the TLS number density is too small to measure while it is not for the BaSrF_2 crystal. (4) As the defect concentration is varied the impurity-induced Raman scattering in the Boson peak region is proportional to that in the LO region while the TLS scattering is not.

All of these results can be accounted for with one model if the disorder parameter is taken quite literally to be a measure of an effective high temperature and the law of mass action is used to describe the number of TLS in this high-temperature equilibrium situation. This disorder is frozen-in presumably during cooling while the crystal is being grown. At high temperatures the superionic conducting anion sublattice provides the natural component that could become pinned out of equilibrium during the cooling process. Applying the law of mass action to the reaction (unassociated TLS + unassociated defect \rightleftharpoons associated defect-TLS complex) gives

$$\frac{p}{(1-p)^2} = zc \exp\left(\frac{T_a}{T_{\text{eff}}}\right), \quad (10)$$

where p equals the degree of association, z represents the number of distinct orientations of the associated complex, cp is the molar concentration of the complex, and kT_a is the Gibbs free energy of association.^{55,56} The quantity to be compared directly with the experimental S_{TLS} values is $c(1-p)$, the molar concentration of the unassociated TLS at a given temperature T_{eff} . Since this effective temperature is proportional to the lattice disorder parameter $|\Delta a/a|$, which is measured, only the constant of proportionality remains to be determined.

The low-temperature line shape of the Raman allowed T_{2g} optic mode in these mixed crystals is quite similar to that found for the pure systems at high temperatures.⁴ Figure 19 shows the comparison for the CaF_2 system. To identify a nonequilibrium temperature our assumption is that when the FWHM of the T_{2g} optic mode for the mixed crystal, $\Delta\omega_d(T_{\text{eff}})$ at 1.4 K equals the FWHM of the pure host, $\Delta\omega_p(T)$ at some elevated temperature T , then this determines the effective temperature of the mixed crystal, i.e., $T_{\text{eff}} \equiv T$. Since we have shown in Fig. 9(a) that $\Delta\omega_d(T_{\text{eff}})$ is directly proportional to the lattice disorder parameter $|\Delta a/a|$ determined from x-ray measurements, then the effective temperature is also proportional to this same parameter. Only the constant of proportionality remains to be determined. In this way we find the effective disorder temperature for all the mixed crystals to be given by

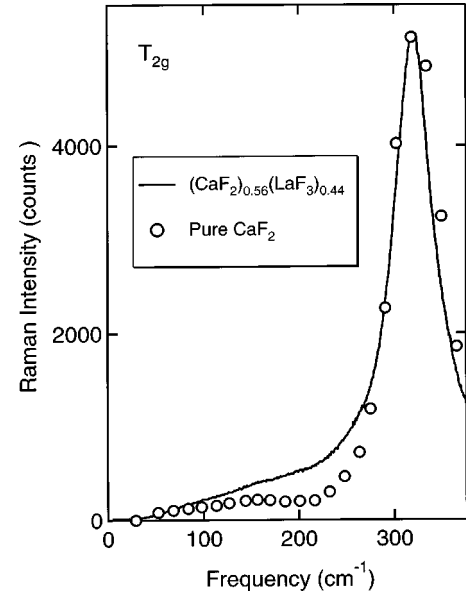


FIG. 19. Comparison of Raman T_{2g} phonon of a fluorite mixed crystal at 1.4 K with that of the pure CaF_2 crystal at an elevated temperature. (The high-temperature data are taken from Ref. 4).

$$T_{\text{eff}} = \frac{1}{\alpha} \left| \frac{\Delta a}{a} \right|. \quad (11)$$

The different α values are listed in column 7, Table II.

In Fig. 20(a), the experimental values for S_{TLS} are compared with least-square fits to $c(1-p)$ obtained from Eq. (10). The three fitting parameters for each curve are listed in columns 8, 9, and 10 in Table II. [Column 11 in Table II illustrates for a specific LaF_3 concentration (5%) how T_{eff}

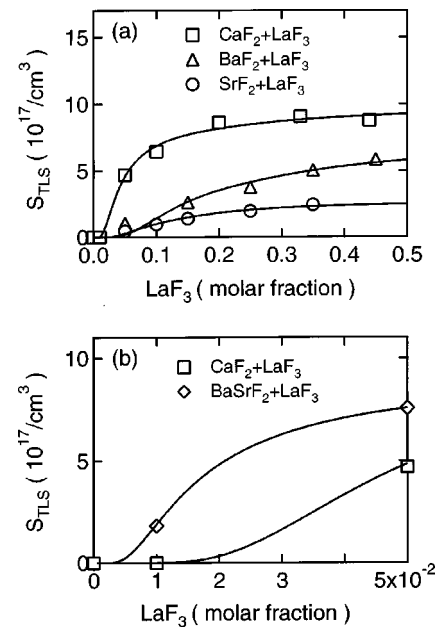


FIG. 20. Experiment and model values for S_{TLS} for three fluorite hosts with LaF_3 impurity, a $(\text{BaSrF}_2)_{0.95}(\text{LaF}_3)_{0.05}$, and a $(\text{BaSrF}_2)_{0.99}(\text{LaF}_3)_{0.01}$ mixed crystal. (a) High concentration region and (b) low concentration region.

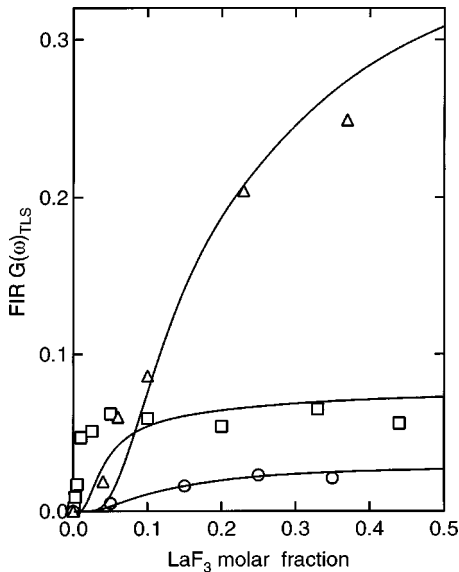


FIG. 21. Concentration dependence of the number density of states times the IR dipole moment squared for the LaF₃ impurity in the three fluorite host lattices. The triangles denote (BaF₂)_{1-x}(LaF₃)_x, the open circles (SrF₂)_{1-x}(LaF₃)_x, and the squares (CaF₂)_{1-x}(LaF₃)_x. These far-IR experimental data are compared with the law of mass action results (solid curves) determined from the Raman experiments. The one new parameter is the IR dipole moment, given in the last column of Table II.

varies with the crystal disorder.] The natural agreement between the high concentration experimental data and the model predictions including the saturation of S_{TLS} for the (CaF₂)_{1-x}(LaF₃)_x mixed crystals is evident.

The absence of Raman-active TLS in the low molar fraction region of (CaF₂)_{1-x}(LaF₃)_x shown in Fig. 20(b) is consistent with the $c(1-p)$ predictions. Note that for the case of (BaSrF₂)_{0.99}(LaF₃)_{0.01}, mixed crystal TLS are indeed detected since the T_{eff} in this case is now much larger. It appears that the LaF₃ doping provides nucleation sites for TLS but that Eq. (10) actually controls S_{TLS} once a sufficient number of nucleation centers are available.

H. Comparison of the Raman and far-IR results on the number density of TLS versus concentration

The observed cutoff frequency of the Raman-active TLS spectrum is about the same as previously observed for the far-IR results and independent of the La³⁺ concentration.¹⁸ Since both the number density per unit frequency range and the total number density of Raman-active TLS are now known and the results described by the law of mass action with an effective disorder temperature, these findings can be compared with the far-IR data for the same crystal systems. By using the far-IR dipole moment as a single parameter for each crystal system, the concentration dependence found for the two different spectroscopic techniques can be compared. The far-IR results $G(\omega)_{\text{TLS}}$ and the law of mass action predictions and solid lines, which agree with the Raman data, are shown in Fig. 21. For SrF₂ and BaF₂ hosts the results are quite close; however, the La doped CaF₂ at low concentra-

tion does not agree either with the Raman data or the law of mass action prediction. This discrepancy is not too surprising since an earlier low concentration far-IR absorption study showed that a set of defect-induced levels, which depended linearly on the La concentration, occurs in this frequency range, and that with increasing dopant concentration these sharp transitions gradually lost strength to a broad TLS distribution, which appeared at higher concentrations.¹⁹ Since the far-IR probe measures both kinds of transitions in this frequency region it is not possible to separate out the TLS contribution of interest here, hence the discrepancy for this particular system at low concentrations.

V. SUMMARY AND CONCLUSIONS

The correlation between the Raman scattering in the boson peak region and in the higher-frequency defect induced E_g resonant mode region connects the boson peak with vibrational properties; however, the fact that the peak moves to higher frequencies with increasing disorder, independent of whether the lattice expands or contracts, is an important new and unexpected signature. These results do not support the proposal that the boson peak in fluorite mixed crystals are resonant vibrational modes in the acoustic region that are quasilocalized in the vicinity of dopant clusters^{24,25} or that it is associated with TLS excited-state transitions. A recent Raman study of TLS in glasses⁵⁷ also shows no correlation between the strengths of the boson peak and the TLS. The experimental results also do not agree with theoretical predictions that increasing the lattice disorder would decrease the frequency of the boson peak or that, in general, the BP frequency is necessarily below the lowest van Hove singularity.^{30,31}

Of the three Raman-active symmetry types present in the fluorite crystal, the low-lying TLS display only A_{1g} symmetry, not E_g or T_{2g} type. In addition, there is no experimental evidence of Raman-active excited-state transitions for such TLS. The strengths of these TLS spectra show distinctive concentration dependencies in the three crystal lattices, with CaF₂ standing out as the most unusual. This same mixed crystal system shows the largest amount of crystal disorder. This result, together with the fact that the low-temperature line shape of the first-order Raman allowed T_{2g} optic mode in these mixed fluorite crystals is quite similar to those previously found for the pure systems at high temperatures,⁴ led us to assign this disorder to an effective temperature. A key result is that the TLS number density is controlled by the law of mass action with the effective temperature determined by the frozen-in lattice disorder. An important universal signature is the absence of TLS below a certain dopant concentration. Because of the nonlinear behavior of Eq. (10) with T_{eff} , the TLS Raman scattering is not proportional to the measured impurity-induced Raman scattering in the LO phonon region. The fact that the TLS scattering and the boson peak have different symmetries, and that they do not scale the same way with defect concentration or with the lattice disorder parameter, is another indication that they involve very different dynamical properties of the disordered solid. The experimentally measured values for S_{TLS} of $\sim 10^{17}/\text{cm}^3$ are

obtained by assuming that the possible orientations of the associated complex are very large ($z > 700$), a result suggesting that such complexes may have many degrees of freedom. It follows that the resulting TLS studied here may be associated with correlated motion of many atoms at low temperatures. It should be noted that this high effective temperature activation picture would be expected to apply to all the high-temperature superionic systems.

In conclusion, our experiments indicate that TLS in the mixed fluorite crystals are a feature of the high-temperature system remaining out of equilibrium upon cooling. The locked in mixed crystal anion lattice disorder simply permits the observation of the high-temperature law of mass action

properties at low temperatures. A feature of the resulting nonequilibrium configuration of the crystal is the TLS spectrum. Although the strength of the Raman-active TLS spectrum depends on the degree of this disorder, the surprise is that its width does not.

ACKNOWLEDGMENTS

The authors thank J. B. Page and R. H. Silsbee for helpful comments and J. A. Campbell for providing many of the samples. Supported in part by NSF-DMR, NASA, and the CCMR facilities.

- ¹R. K. Chang, W. B. Lacina, and P. S. Pershan, *Phys. Rev. Lett.* **17**, 755 (1966).
- ²W. B. Lacina and P. S. Pershan, *Phys. Rev. B* **1**, 1765 (1970).
- ³L. L. Chase, D. Kühner, and W. E. Bron, *Phys. Rev. B* **7**, 3892 (1973).
- ⁴R. J. Elliott, W. Hayes, W. G. Kleppmann, A. J. Rushworth, and J. F. Ryan, *Proc. R. Soc. London, Ser. A* **360**, 317 (1978).
- ⁵W. Hayes, in *Light Scattering in Solids III*, edited by M. Cardona and G. Güntherodt (Springer, Berlin, 1982), p. 93.
- ⁶D. van der Marel and H. W. den Hartog, *Phys. Rev. B* **25**, 6602 (1982).
- ⁷D. J. Oostra and H. W. den Hartog, *Phys. Rev. B* **29**, 2423 (1984).
- ⁸F. J. Walker and A. C. Anderson, *Phys. Rev. B* **29**, 5881 (1984).
- ⁹S. K. Kazanskii, *JETP Lett.* **41**, 224 (1985).
- ¹⁰R. C. Zeller and R. O. Pohl, *Phys. Rev. B* **4**, 2029 (1971).
- ¹¹P. W. Anderson, B. I. Halperin, and C. M. Varma, *Philos. Mag.* **25**, 1 (1972).
- ¹²W. A. Phillips, *J. Low Temp. Phys.* **7**, 351 (1972).
- ¹³W. A. Phillips, *Rep. Prog. Phys.* **50**, 1657 (1987).
- ¹⁴D. G. Cahill and R. O. Pohl, *Phys. Rev. B* **39**, 10 477 (1989).
- ¹⁵K. A. Topp and D. G. Cahill, *Z. Phys. B: Condens. Matter* **101**, 235 (1996).
- ¹⁶K. A. Topp, E. Thompson, and R. O. Pohl, *Phys. Rev. B* **60**, 898 (1999).
- ¹⁷S. A. FitzGerald, J. A. Campbell, and A. J. Sievers, *Phys. Rev. Lett.* **73**, 3105 (1994).
- ¹⁸S. A. FitzGerald, A. J. Sievers, and J. A. Campbell, *J. Phys. C* **13**, 2177 (2001).
- ¹⁹S. A. FitzGerald, A. J. Sievers, and J. A. Campbell, *J. Phys. C* **13**, 2095 (2001).
- ²⁰J. J. Tu, J. A. Campbell, and A. J. Sievers, *Bull. Am. Phys. Soc.* **41**, 549 (1996).
- ²¹J. J. Tu, S. A. FitzGerald, J. A. Campbell, and A. J. Sievers, *J. Non-Cryst. Solids* **203**, 153 (1996).
- ²²J. J. Tu and A. J. Sievers, *Phys. Rev. Lett.* **83**, 4077 (1999).
- ²³S. P. Love, C. E. Mungan, A. J. Sievers, and J. Campbell, *J. Opt. Soc. Am. B* **9**, 794 (1992).
- ²⁴M. Kolesik, D. Tunega, and B. P. Sobolev, *Phys. Status Solidi B* **160**, 375 (1990).
- ²⁵M. Kolesik, D. Tunega, and B. P. Sobolev, *Solid State Ionics* **58**, 237 (1992).
- ²⁶J. Jäckle, in *Amorphous Solids*, edited by W. A. Phillips (Springer, Berlin, 1981).
- ²⁷A. P. Sokolov, A. Kisliuk, D. Quitmann, and E. Duval, *Phys. Rev. B* **48**, 7692 (1993).
- ²⁸S. R. Elliott, *Physics of Amorphous Materials* (Wiley, New York, 1990).
- ²⁹A. P. Sokolov, A. Kisliuk, M. Soltwisch, and D. Quitmann, *Phys. Rev. Lett.* **69**, 1540 (1992).
- ³⁰W. Schirmacher, G. Diezemann, and C. Ganter, *Phys. Rev. Lett.* **81**, 136 (1998).
- ³¹S. N. Taraskin, Y. L. Loh, G. Natarajan, and S. R. Elliott, *Phys. Rev. Lett.* **86**, 1255 (2001).
- ³²W. Hayes, *Crystals with the Fluorite Structure* (Clarendon, Oxford, 1974).
- ³³R. Shuker and R. W. Gammon, *Phys. Rev. Lett.* **25**, 222 (1970).
- ³⁴W. Hayes and R. Loudon, *Scattering of Light by Crystals* (Wiley, New York, 1978).
- ³⁵A. S. Barker and A. J. Sievers, *Rev. Mod. Phys.* **47**, FS1 (1975).
- ³⁶L. Vegard, *Z. Phys.* **5**, 17 (1921).
- ³⁷N. Theodorakopoulos and J. Jäckle, *Phys. Rev. B* **14**, 2637 (1976).
- ³⁸A. E. Hughes, *Solid State Commun.* **6**, 61 (1968).
- ³⁹A. E. Hughes, *J. Phys. Chem. Solids* **29**, 1461 (1968).
- ⁴⁰J. D. Eshelby, *Solid State Phys.* **3**, 79 (1956).
- ⁴¹R. W. Alexander, Ph.D. thesis, Cornell University, 1968 (unpublished).
- ⁴²R. T. Harley, J. B. Page, and C. T. Walker, *Phys. Rev. B* **3**, 1365 (1971).
- ⁴³B. P. Clayman, I. G. Nolt, and A. J. Sievers, *Phys. Rev. Lett.* **19**, 111 (1967).
- ⁴⁴D. N. Payton and W. M. Visscher, *Phys. Rev.* **175**, 1201 (1968).
- ⁴⁵J. B. Page, *Phys. Rev. B* **10**, 719 (1974).
- ⁴⁶R. A. Cowley, in *The Raman Effect*, edited by A. Anderson (Marcel Dekker, New York, 1971), Vol. 1.
- ⁴⁷M. V. Klein, in *Dynamical Properties of Solids*, edited by A. A. Maradudin and G. K. Horton (North Holland, Amsterdam, 1990), Vol. VI.
- ⁴⁸S. K. Watson, *Phys. Rev. Lett.* **75**, 1965 (1995).
- ⁴⁹P. S. Goyal, S. L. Narasimhan, A. Inaba, W. Kagunya, and C. J. Carlile, *Europhys. Lett.* **39**, 509 (1997).
- ⁵⁰S. K. Watson, D. G. Cahill, and R. O. Pohl, *Phys. Rev. B* **40**, 6381 (1989).

- ⁵¹J. J. De Yoreo, W. Knaak, M. Meissner, and R. O. Pohl, Phys. Rev. B **34**, 8828 (1986).
- ⁵²D. Moy, J. N. Dobbs, and A. C. Anderson, Phys. Rev. B **29**, 2160 (1984).
- ⁵³A. M. Kahan, Ph.D. thesis, Cornell University, 1973 (unpublished).
- ⁵⁴F. Bridges, M. Recce, and M. Morgan, Radiat. Eff. **73**, 31 (1983).
- ⁵⁵A. B. Lidiard, in *Handbuch der Physik*, edited by S. Flügge (Springer, Berlin, 1957), Vol. 20, p. 246.
- ⁵⁶A. R. Allnatt and A. B. Lidiard, *Atomic Transport in Solids* (Cambridge University Press, Cambridge, 1993), p. 572.
- ⁵⁷J. J. Tu and A. J. Sievers, Phys. Rev. B **65**, 144204 (2002).